Optimal Control of Short-Time Attractors in Active Nematics

Carlo Sinigaglia and Francesco Braghin
Politecnico di Milano, Department of Mechanical Engineering, 20156, Italy

Mattia Serra*
University of California San Diego, Department of Physics, CA 92093, USA
(Dated: April 24, 2024)

Objective Eulerian Coherent Structures (OECSs) and instantaneous Lyapunov exponents (iLEs) govern short-term material transport in fluid flows as Lagrangian Coherent Structures and the Finite-Time Lyapunov Exponent do over longer times. Attracting OECSs and iLEs reveal short-time attractors and are computable from the Eulerian rate-of-strain tensor. Here, we devise for the first time an optimal control strategy to create short-time attractors in compressible, viscosity-dominated active nematic flows. By modulating the active stress intensity, our framework achieves a target profile of the minimum eigenvalue of the rate-of-strain tensor, controlling the location and shape of short-time attractors. We use numerical simulations to show that our optimal control strategy effectively achieves desired short-time attractors while rejecting disturbances. Combining optimal control and coherent structures, our work offers a new perspective to steer material transport in compressible active nematics, with applications to morphogenesis and synthetic active matter.

Large-scale coherent dynamics where global collective behaviors arise from local interactions, individual anisotropies and activity are ubiquitous. Bird flocks, bacterial swarms or ensembles of cells exhibit macroscopic patterns whose length scale is orders of magnitude larger than the individual size [1–6]. The macroscopic dynamics of these systems of active individuals –or active matter– exhibit nonstandard physical properties such as self-organization, symmetry breaking and nonreciprocity [2, 7–10]. There are several descriptions of active matter [11], including agent-based models, coarse-grained continuum models, and data-driven models [12]. Besides studying the emergent properties of active matter, it is natural to ask how to control such systems.

The main possibilities rely on distributed or boundary control techniques [13]. Experimentally, Ross et al. [14] generated desired persistent fluid flows by regulating light patterns on a mixture of optogenetically modified motor proteins and microtubule filaments. Also controlling light, Lemma et al. [15] achieved spatiotemporal patterning of extensile active stresses in microtubule-based active fluids. By controlling an external electric field affecting cellular signaling networks, Cohen et al. [16] steered the collective motion of MDCK-II epithelial cells. From a theoretical perspective, Shankar et al. [17] propose a new framework to steer topological defects –the localized singularities in the orientation of the active building blocks [2]– by controlling activity stress patterns. Norton et al. [18] devised an Optimal Control Problem (OCP) to achieve a target nematic director field by controlling either an applied vorticity field or the active stress magnitude in incompressible active nematics. Alternative control strategies use surface anchoring at the boundaries and substrate drag to rectify the coherent flow of an active polar fluid in a 2D channel [19].

Existing theoretical methods target a desired configuration of the nematic director field, topological defects or fluid velocities. While defects' dynamics drive large-scale chaotic flow [21–23], they may not be enough to predict spatiotemporal material transport. For instance, Serra et al. [24] show in experimental and numerical active nematics that the director field alone cannot predict if different domain regions will mix over a desired time interval or remain separated by a transport barrier, as well as predict where transport barriers are. In fact, even the knowledge of the velocity field and typical streamline or vorticity plots are sub-optimal to studying material transport in unsteady flows, as shown in experimental and simulated velocities [25–27] and Figure 1.

A natural framework to quantify material transport is the concept of Coherent Structures (CSs), see e.g. [25, 26, 28], which serve as the robust frame-invariant skeletons shaping complex trajectory patterns. CSs such as attractors, their domain of attraction and repellers are widespread in embryonic development across species [29–31] and active nematics [24]. Here, we devise for the first time an optimal control strategy to create short-time attractors in compressible, viscosity-dominated active nematic flows [30, 32]. While most theory literature on active matter control assumes incompressible flows, in gastrulation and morphogenesis, flows are highly compressible, accounting for the internalization of cells to start organogenesis.

I. MATERIAL TRANSPORT

Long-term material transport is a Lagrangian phenomenon, originally studied by tracking the redistribution of individual trajectories. In that setting, the Finite Time Lyapunov Exponent (FTLE) and Lagrangian coherent structures (LCSs) successfully predicted material transport [24, 25, 28, 29, 33, 34]. An alternative to La-

* mserra@ucsd.edu

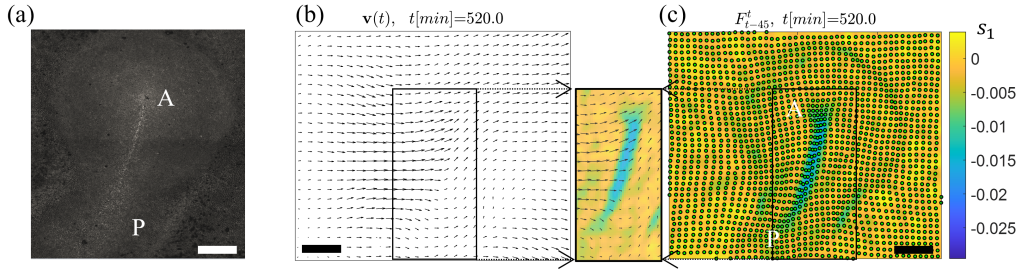

FIG. 1. Short-time attractors in an experimental multicellular flow. (a) Fluorescence image of the chicken embryo's epiblast, containing $\approx 60,000$ cells during gastrulation. AP denotes the Anterior-Posterior axis. Velocities are reconstructed from Light Sheet Microscopy [20]. The scale bar is $500\mu m$, and $t = 0$ corresponds to the beginning of gastrulation. (b) Velocity field $\mathbf{v}(\mathbf{x}, 520)$ (black vectors). (c) Instantaneous Lyapunov Exponent field $s_1(\mathbf{x}, 520)$ (colormap), consisting of the smallest eigenvalue of the rate-of-strain tensor of $\mathbf{v}$. Negative values of $s_1(\mathbf{x}, 520)$ mark short-time attractors. To visualize the effect of short-term attractors, green dots in panel c mark the current $t = 520$ position $\mathbf{F}^{520}_{475}(\mathbf{x_0}) = \mathbf{x_0} + \int^{520}_{475} \mathbf{v}(\mathbf{F}^{\tau}_{475}, \tau)d\tau$ of short-time trajectories of $\mathbf{v}(\mathbf{x}, t)$, starting at $t = 475$ from a uniform spatial configuration. Within this short time ($45\ min/12h \approx 6\%$ of gastrulation time), trajectories accumulate on the $s_1(\mathbf{x}, 520)$ trench. The inset shows both $\mathbf{v}(\mathbf{x}, 520)$ and $s_1(\mathbf{x}, 520)$, highlighting how attractors remain hidden to $\mathbf{v}$ but are correctly captured by s_1. See Fig. S2 for the same analysis at a different time.

grangian approaches is to find their instantaneous limits purely from Eulerian observations, avoiding the pitfalls of trajectory integration. Additionally, LCSs are impractical to control–no literature exists–because they are defined as nonlinear functions of fluid trajectories, which are integrals of the Eulerian velocity $\mathbf{v}$.

Short-time attractors – originally defined as Attracting OECSs [26] – govern material transport in fluid flows over short-times, revealing critical information in challenging problems such as search and rescue operations at sea [27] and oil-spill containment [35]. A simpler, more controllable alternative to attracting OECSs for locating short-time attractors is the instantaneous Lyapunov Exponent (iLE)[36], defined as the instantaneous limit of the well-known FTLE. The iLE locates short-time attractors as trenches – or negative regions – of the smallest eigenvalue s_1 of the rate-of-strain tensor of the fluid velocity. For example, Fig.1 shows short-term attractors marked by trenches of s_1 (scalar field) in an experimental velocity field (black vectors) describing the motion of thousands of cells during chick gastrulation [20]. A strong trench of s_1 marks a short-term attractor along the anterior-posterior (AP) axis corresponding to the forming primitive streak [29] (panel c), while remaining not identifiable from the inspection of the corresponding velocity field (panel b and inset). Similar results hold in different flows (e.g., Fig. 1 of [26] and Figs. 4-5 of [27]).

This example shows that inspection and control of the velocity field $\mathbf{v}$ is sub-optimal to create material traps in general unsteady flows. First, because the velocity field and its streamlines are not objective, i.e., they depend on the choice of reference frame used to describe motion (see also SM Section 6 and Figs. S1-S2). By contrast, the location of material accumulation is frame invariant [25, 26]. Second, it might be an unnecessarily strong requirement, or uncompliant with boundary conditions, to prescribe $\mathbf{v}(\mathbf{x}, t)$ directly.

II. ACTIVE FLUID MODEL

We adopt a simplified version of the mechanochemical model developed in [30] consisting of an active stokes flow characterized by the viscous stress $\sigma_v = -p\mathbf{I} + 2\mu\mathbf{S}_d$ and active stress $\sigma_a = m(\mathbf{B} - \mathbf{I}/2)$, where $\mathbf{S}_d$ is the deviatoric rate-of-strain tensor, $\mathbf{B} = \mathbf{e}\otimes\mathbf{e}$ characterizes the orientation of active elements $\mathbf{e} = (\cos(\phi)\ \sin(\phi))^\top$, m denotes the intensity of active stress and $\mathbf{I}$ the identity tensor. To account for flow compressibility, we use a simple continuity equation $\nabla\cdot\mathbf{v} = c(-2p - p_0 m)$ where positive isotropic viscous stress ($p > 0$), and isotropic contractile-type ($m > 0$) active stress contribute to negative flow divergence via the bulk viscosity $1/c$ and a nondimensional parameter p_0. Biologically, p_0 modulates the cell propensity to ingress into the third dimension given active isotropic apical contraction. The resulting system of PDEs in nondimensional form [30] is

$$\begin{aligned}
&2p_1\Delta\mathbf{v} + \nabla[\nabla\cdot\mathbf{v}] + \mathbf{g}(m,\phi) = \mathbf{0},\\
&\mathbf{g} = p_1[2(\mathbf{B}\nabla m + m\nabla\cdot\mathbf{B}) + (p_0 - 1)\nabla m] = \nabla\cdot(\mathbf{A}m),\\
&\phi_t = -(\mathbf{v}\cdot\nabla)\phi + \tfrac{\omega}{2} + \left(\tfrac{u_y+v_x}{2}\cos 2\phi + \tfrac{v_y-u_x}{2}\sin 2\phi\right),\\
&m_t = -(\mathbf{v}\cdot\nabla)m + p_2(1 - me^{-\frac{p_3}{2}m}) + p_4\Delta m,
\end{aligned} \tag{1}$$

where $p_1 = \mu c$ is a second nondimensional parameter characterizing the ratio of the shear to bulk viscosity, $\mathbf{g}(m,\phi)$ is the active force, and $\mathbf{A} = 2p_1\mathbf{B} + p_1(p_0 - 1)\mathbf{I}$. The last two equations–not used here–model the dynamics of the active stress intensity and orientation coupled to the tissue velocity [30, 32]. In biological flows dominated by active stresses, one expects the nondimensional $|m|$ characterizing the ratio of active to viscous stresses to achieve values of order 10 as in [30].

Abstracting morphogenesis as a control problem, one can ask how embryos control their active stress to bring the right cells to specific spatiotemporal coordinates. This is precisely the case shown in Fig. 1, where mesendoderm precursor cells converge to the attractors,

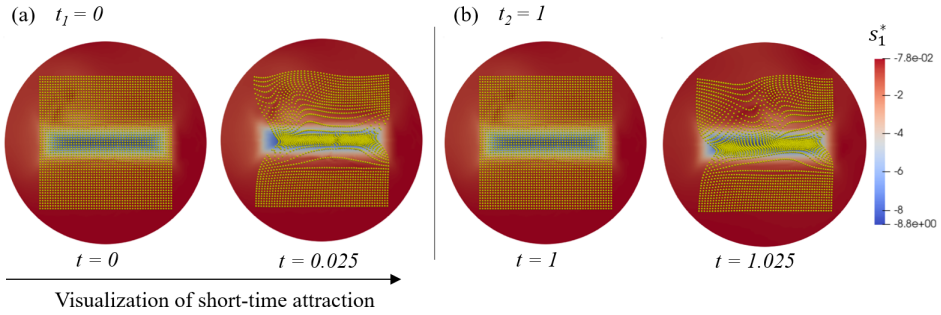

FIG. 2. Optimal solution of the OCP generating short-time attractors. The target minimum eigenvalue $z(\mathbf{x})$ is the indicator function of a rectangle at the center of the domain. The optimal eigenvalue field $s_1^\star(\mathbf{x})$ is shown by the colormap. a-b correspond to different initialization times t_i and show the effect of short-time attractors by initializing a uniform set of fluid tracers (yellow dots) at each t_i and displaying their later positions integrating $\mathbf{v}(\mathbf{x}, t)$ over short times, as in Figs. 1c.

marking the primitive streak [30]. As a first step, we consider a simplified dynamic where the orientation of active elements $\phi(\mathbf{x})$ is prescribed and time-independent, and use the active stress intensity $m(\mathbf{x}, t)$ as the control input. A time-independent ϕ is a simplification that could be experimentally enforced by steady morphogen concentration inducing planar cell polarity or by imposing directional tension at the boundary [37]. How one might control m experimentally is system-dependent. In microtubule-based active fluids, m can be controlled with light patterns [15]. By contrast, in the context of gastrulation–the most pertinent for our approach, given the viscous, compressible active nematic model (Eq. 1)–we were able to indirectly control m in-vivo in chick embryos by adding FGF2 (fibroblast growth factor 2) (see e.g., Fig. 4 of [30] and [32], and SM S8). In Drosophila, m can be modulated by optogenetic activation or inhibition of Rho signaling [38–41].

III. RESULTS

To control short-time attractors, the OCP involves steering the minimum eigenvalue of the rate of strain tensor towards a target function while minimizing the overall control effort and its gradient:

$$\min_{m,\mathbf{v}} \; J_s = \frac{1}{2}\int_\Omega (s_1 - z)^2 \, d\Omega + \frac{\beta}{2}\int_\Omega \left(m^2 + \|\nabla m\|^2\right) d\Omega,$$

$$s.t. \quad \begin{aligned} -2p_1\Delta\mathbf{v} - \nabla[\nabla\cdot\mathbf{v}] &= \mathbf{g}(m) + \mathbf{d} \quad \text{in} \quad \Omega \\ \mathbf{v} &= \mathbf{0} \qquad\qquad\quad \text{on} \quad \partial\Omega, \end{aligned} \tag{2}$$

where $z(\mathbf{x})$ represents a scalar target for the minimum eigenvalue $s_1(\mathbf{x})$ of the rate-of-strain tensor $\mathbf{S}$, $\mathbf{d}(\mathbf{x}, t)$ is an imposed known force (or disturbance), and $\Omega, \partial\Omega$ denote the domain and its boundary, where we impose $\mathbf{v} = \mathbf{0}$. In morphogenesis, $\mathbf{d}$ could arise from external forces imposed on, rather than controlled by, the embryo. The optimal pair $(\mathbf{v}, m)$ for the OCP (2) should satisfy the following system of first-order necessary conditions

$$\begin{aligned} -2p_1\Delta\mathbf{v} - \nabla[\nabla\cdot\mathbf{v}] &= \mathbf{g}(m) + \mathbf{d} && \text{in} \quad \Omega \\ \mathbf{v} &= \mathbf{0} && \text{on} \quad \partial\Omega \\ -2p_1\Delta\boldsymbol{\lambda} - \nabla[\nabla\cdot\boldsymbol{\lambda}] &= -\nabla\cdot\Big((s_1 - z)\,\boldsymbol{\xi}_1 \otimes \boldsymbol{\xi}_1\Big) && \text{in} \quad \Omega \\ \boldsymbol{\lambda} &= \mathbf{0} && \text{on} \quad \partial\Omega \\ -\beta\Delta m + \beta m - \nabla\boldsymbol{\lambda} : \mathbf{A} &= 0 && \text{in} \quad \Omega, \end{aligned} \tag{3}$$

where $\boldsymbol{\xi}_1$ is the eigenvector field associated with s_1 (SM Sections 2-4 for details). Practically, at any t, given an imposed force distribution $\mathbf{d}(\mathbf{x}, t)$, boundary conditions and desired short-time attractor $z(\mathbf{x})$, (3) generates the optimal $m(\mathbf{x}, t)$ to achieve z. See SM Sec. 8 for an algorithmic summary of (3) and a concrete application to avian-embryos morphogenesis. Eq. (3) requires an iterative method due to the complex nonlinear relationship between $\mathbf{v}$ and the forcing term of the adjoint equation involving s_1 and $\boldsymbol{\xi}_1$. We solve (3) using a Finite Element Method (FEM) and a gradient-based algorithm (SM Sec. 5) on a circular domain, and note that our algorithm applies to arbitrary domains.

We set the target shape z as a scaled indicator function of a rectangle so that the target value is -10 inside the rectangle and zero elsewhere. We set the cable orientation to a constant value $\phi = \frac{\pi}{4}$ from the x-axis and choose the control weighting parameter $\beta = 10^{-6}$ and the nondimensional model parameters $p_0 = 10$, $p_1 = 0.5$. p_1 modulates the overall fluid compressibility while high p_0 induces high negative divergence in regions with higher m [30]. We select the space-time varying disturbance force as $\mathbf{d}(\mathbf{x}, t) = d\, e^{-(\frac{r(t)}{\sigma})^2}\,[-(y - y_c(t)), x - x_c(t)]$, where $\mathbf{x}_c(t) = [-0.5 + t, 0.5]$, $r(t) = ||\mathbf{x} - \mathbf{x}_c(t)||$, and set the intensity $d = 50$, and standard deviation $\sigma = 0.2$. Figure 2 shows the resulting optimal s_1 along with a grid of particles advected over short times for two different initialization times. Figure 3 shows the optimal state-control pair and its associated disturbance $\mathbf{d}$. The control m acts through $\mathbf{g}(m) = \nabla\cdot(\mathbf{A}m)$, and therefore both m and ∇m contribute to the state dynamics. Overall the disturbance strongly influences the optimal velocity.

Figure 4 shows the interplay between the control

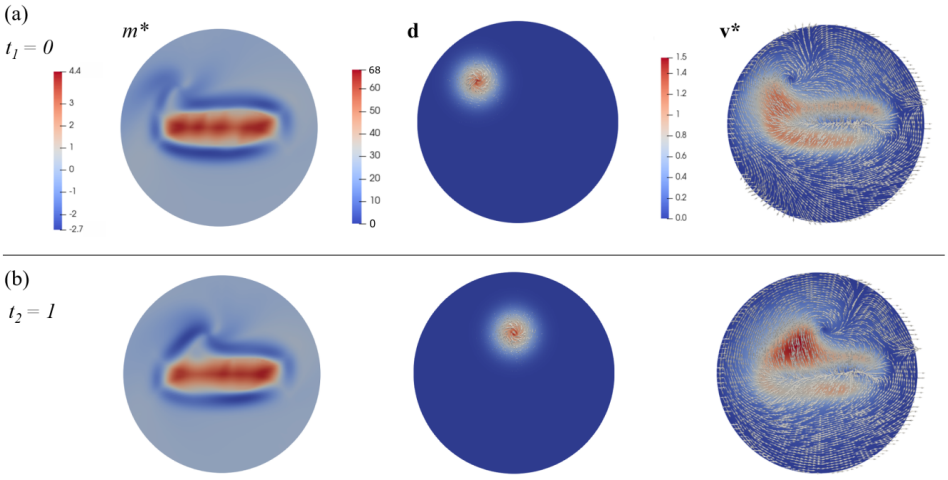

FIG. 3. Optimal control state pair $(m^\star, \mathbf{v}^\star)$ and moving imposed (or disturbance) $\mathbf{d}$ associated to the OCP described in Fig. 2. $\mathbf{d}$ and $\mathbf{v}^\star$ are vector fields (arrows) with their magnitude also displayed in the colormap. The $\mathbf{v}^\star$ vectors are normalized to ease visualization. Each row (a-b) corresponds to different initialization times t_i as Fig. 2. The velocity dynamics $\mathbf{v}$ are strongly affected by the presence of the disturbance.

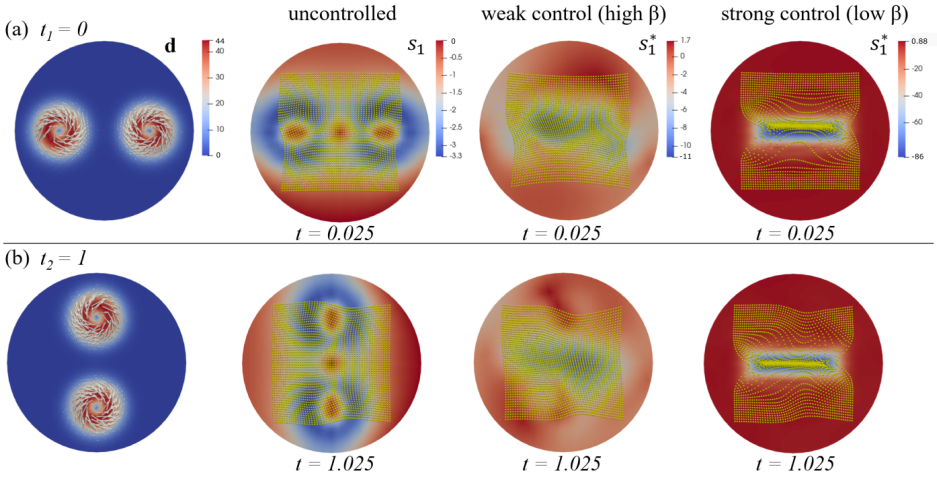

FIG. 4. Controlled and uncontrolled dynamics for two spatiotemporal disturbances $\mathbf{d}(\mathbf{x}, t_i)$ (first column). Columns 2-4 show $s_1(\mathbf{x})$ for no control, weak ($\beta = 0.1$) and strong ($\beta = 10^{-6}$) control along with fluid tracers advected for a short time starting from a uniform initial grid at t_i. Here, $\mathbf{d}(\mathbf{x}, t) = \mathbf{d}(\mathbf{x}_{c1}(t)) - \mathbf{d}(\mathbf{x}_{c2}(t))$, where $\mathbf{x}_{c1}(t) = 0.5[\cos(0.5\pi t + \pi), \cos(0.5\pi t + \pi)]$, $\mathbf{x}_{c2}(t) = 0.5[\cos(0.5\pi t), \cos(0.5\pi t)]$, and $\mathbf{d}(\mathbf{x}_{ci}(t)) = [-(y - y_{ci}(t)), (x - x_{ci}(t))]500\exp(-((x - x_{ci}(t))^2 + (y - y_{ci}(t)^2))/0.2^2$.

weight β, the disturbance $\mathbf{d}$ and the accuracy of the tracking objective. To present an additional test case, we select a different disturbance compared to Figs. 2-3, generating two vortex-shaped force-field streamlines (Figure 4, first column) using the same functional form in the previous test case. The target eigenvalue z is the same as in Figs. 2-3. The uncontrolled dynamics ($m = 0$) does not generate attraction (Figure 4, second column), while weak and strong control (third-fourth columns) steer s_1 towards the target, generating a material trap while rejecting $\mathbf{d}$. In SM S7, we provide an extensive sensitivity analysis and show that our control scheme can generate any attractor geometry and is robust to changes in control and model parameters, the orientation of active elements ϕ, and the disturbance $\mathbf{d}$. In SM S8, we illustrate our approach in the context of avian gastrulation control, where $\mathbf{d}$ represents a traction force imposed on the embryo by extraembryonic cells, and the embryo develops a ring-shaped, short-time attractor by modulating its active myosin distribution m, consistent with in-vivo experiments in the chick embryo [30, 32].

IV. CONCLUSION

We have proposed an optimal control problem that generates, for the first time, material short-time attractors at desired locations in compressible, highly viscous

active nematics using the active stress intensity as the control input. Short-time attractors predict the correct location of material attraction, which may be undetected from the inspection of frame-dependent velocity fields (Fig. 1, [26, 27]). Additionally, several configurations of the frame-dependent $\mathbf{v}$ can generate the same frame-invariant attractor configurations (see e.g. Figs. S3-5). Similarly, one can control material repellers, which, together with attractors, shape complex motion in synthetic active matter [24] and living embryos [29, 31]. Our results demonstrate how to achieve these aims in principal. As experimental techniques to manipulate m increase in their precision and availability in more systems, this theoretical technique may enable the creation of material traps for medical applications as well as enhance our ability to control morphogenetic flows. For example, it will shed light on how myosin activity (active stress intensity) generates the required motion that compartmentalizes the embryo, segregating distinct cell types (repellers) and steering specific cells to precise locations (attractors). In future work, we plan to consider the explicit orientational dynamics of the active stress anisotropy, the effect of inertial forces, and the control of Lagrangian Coherent Structures that shape fluid motion over longer times.

ACKNOWLEDGMENTS

We acknowledge Manli Chuai, Guillermo Serrano Nájera and Kees Weijer for the experimental data in Fig. 1 and SM S8, and Alex Plum for his comments on the manuscript.

[1] J. Toner and Y. Tu, Long-range order in a two-dimensional dynamical XY model: How birds fly together, Physical Review Letters **75**, 4326 (1995).
[2] M. C. Marchetti, J. F. Joanny, S. Ramaswamy, T. B. Liverpool, J. Prost, M. Rao, and R. A. Simha, Hydrodynamics of soft active matter, Rev. Mod. Phys. **85**, 1143 (2013).
[3] K. Kruse, J. Joanny, F. Jülicher, J. Prost, and K. Sekimoto, Asters, vortices, and rotating spirals in active gels of polar filaments, Physical review letters **92**, 078101 (2004).
[4] M. Ballerini, N. Cabibbo, R. Candelier, A. Cavagna, E. Cisbani, I. Giardina, V. Lecomte, A. Orlandi, G. Parisi, A. Procaccini, *et al.*, Interaction ruling animal collective behavior depends on topological rather than metric distance: Evidence from a field study, Proceedings of the national academy of sciences **105**, 1232 (2008).
[5] A. Bricard, J. Caussin, N. Desreumaux, O. Dauchot, and D. Bartolo, Emergence of macroscopic directed motion in populations of motile colloids, Nature **503**, 95 (2013).
[6] C. Dombrowski, L. Cisneros, S. Chatkaew, R. Goldstein, and J. Kessler, Self-concentration and large-scale coherence in bacterial dynamics, Physical review letters **93**, 098103 (2004).
[7] S. Ramaswamy, Active matter, Journal of Statistical Mechanics: Theory and Experiment **2017**, 054002 (2017).
[8] M. Fruchart, R. Hanai, P. B. Littlewood, and V. Vitelli, Non-reciprocal phase transitions, Nature **592**, 363 (2021), arXiv:2003.13176.
[9] M. J. Bowick, N. Fakhri, M. C. Marchetti, and S. Ramaswamy, Symmetry, thermodynamics, and topology in active matter, Physical Review X **12**, 010501 (2022).
[10] S. Shankar, A. Souslov, M. J. Bowick, M. C. Marchetti, and V. Vitelli, Topological active matter, Nature Reviews Physics **4**, 380 (2022).
[11] M. R. Shaebani, A. Wysocki, R. G. Winkler, G. Gompper, and H. Rieger, Computational models for active matter, Nature Reviews Physics **2**, 181 (2020).
[12] C. Joshi, S. Ray, L. M. Lemma, M. Varghese, G. Sharp, Z. Dogic, A. Baskaran, and M. F. Hagan, Data-driven discovery of active nematic hydrodynamics, Physical review letters **129**, 258001 (2022).
[13] A. Manzoni, S. Salsa, and A. Quarteroni, *Optimal Control of Partial Differential Equations, Analysis, Analysis, Approximation and Applications* (Springer, 2021).
[14] T. D. Ross, H. J. Lee, Z. Qu, R. A. Banks, R. Phillips, and M. Thomson, Controlling organization and forces in active matter through optically defined boundaries, Nature **572**, 224 (2019).
[15] L. M. Lemma, M. Varghese, T. D. Ross, M. Thomson, A. Baskaran, and Z. Dogic, Spatio-temporal patterning of extensile active stresses in microtubule-based active fluids, PNAS nexus **2**, pgad130 (2023).
[16] D. J. Cohen, W. James Nelson, and M. M. Maharbiz, Galvanotactic control of collective cell migration in epithelial monolayers, Nature materials **13**, 409 (2014).
[17] S. Shankar, L. V. Scharrer, M. J. Bowick, and M. C. Marchetti, Spatiotemporal control of active topological defects, arXiv preprint arXiv:2212.00666 (2022).
[18] M. M. Norton, P. Grover, M. F. Hagan, and S. Fraden, Optimal control of active nematics, Physical review letters **125**, 178005 (2020).
[19] P. Gulati, S. Shankar, and M. C. Marchetti, Boundaries control active channel flows, Frontiers in Physics **10**, 10.3389/fphy.2022.948415 (2022).
[20] E. Rozbicki, M. Chuai, A. Karjalainen, F. Song, H. Sang, R. Martin, H. Knölker, M. MacDonald, and C. Weijer, Myosin-II-mediated cell shape changes and cell intercalation contribute to primitive streak formation, Nat Cell Biol **17**, 397 (2015).
[21] L. Giomi, Geometry and topology of turbulence in active nematics, Phys. Rev. X **5**, 031003 (2015).
[22] S. Shankar and M. C. Marchetti, Hydrodynamics of active defects: From order to chaos to defect ordering, Phys. Rev. X **9**, 041047 (2019).
[23] A. J. Tan, E. Roberts, S. A. Smith, U. A. Olvera, J. Arteaga, S. Fortini, K. A. Mitchell, and L. S. Hirst, Topological chaos in active nematics, Nature Physics **15**, 1033 (2019).
[24] M. Serra, L. Lemma, L. Giomi, Z. Dogic, and L. Mahadevan, Defect-mediated dynamics of coherent structures in active nematics, arXiv preprint arXiv:2104.02196, to appear in Nature Physics (2023).

[25] G. Haller, Lagrangian coherent structures, Annu. Rev. Fluid Mech **47**, 137 (2015).

[26] M. Serra and G. Haller, Objective eulerian coherent structures, Chaos: An Interdisciplinary Journal of Nonlinear Science **26**, 053110 (2016).

[27] M. Serra, P. Sathe, I. Rypina, A. Kirincich, S. D. Ross, P. Lermusiaux, A. Allen, T. Peacock, and G. Haller, Search and rescue at sea aided by hidden flow structures, Nature communications **11**, 1 (2020).

[28] A. Hadjighasem, M. Farazmand, D. Blazevski, G. Froyland, and G. Haller, A critical comparison of Lagrangian methods for coherent structure detection, Chaos **27**, 053104 (2017).

[29] M. Serra, S. Streichan, M. Chuai, C. J. Weijer, and L. Mahadevan, Dynamic morphoskeletons in development, Proceedings of the National Academy of Sciences **117**, 11444 (2020).

[30] M. Serra, G. Serrano Nájera, M. Chuai, A. M. Plum, S. Santhosh, V. Spandan, C. J. Weijer, and L. Mahadevan, A mechanochemical model recapitulates distinct vertebrate gastrulation modes, Science Advances **9**, eadh8152 (2023).

[31] M. Lange, A. Granados, S. VijayKumar, J. Bragantini, S. Ancheta, S. Santhosh, M. Borja, H. Kobayashi, E. McGeever, A. C. Solak, *et al.*, Zebrahub-multimodal zebrafish developmental atlas reveals the state transition dynamics of late vertebrate pluripotent axial progenitors, bioRxiv , 2023 (2023).

[32] M. Chuai, G. Serrano Nájera, M. Serra, L. Mahadevan, and C. J. Weijer, Reconstruction of distinct vertebrate gastrulation modes via modulation of key cell behaviors in the chick embryo, Science Advances **9**, eabn5429 (2023).

[33] S. Shadden, F. Lekien, and J. E. Marsden, Definition and properties of Lagrangian coherent structures from finite-time Lyapunov exponents in two-dimensional aperiodic flows, Physica D **212**, 271 (2005).

[34] M. Serra, P. Sathe, F. Beron-Vera, and G. Haller, Uncovering the Edge of the Polar Vortex, J. Atmos. Sci. **74**, 3871 (2017).

[35] R. Duran, T. Nordam, M. Serra, and C. H. Barker, Horizontal transport in oil-spill modeling, in *Marine Hydrocarbon Spill Assessments* (Elsevier, 2021) pp. 59–96.

[36] P. J. Nolan, M. Serra, and S. D. Ross, Finite-time Lyapunov exponents in the instantaneous limit and material transport, Nonlinear Dynamics **100**, 3825 (2020), arXiv:1904.06817.

[37] D. Kunz, A. Wang, C. U. Chan, R. H. Pritchard, W. Wang, F. Gallo, C. R. Bradshaw, E. Terenzani, K. H. Müller, Y. Y. S. Huang, *et al.*, Downregulation of extraembryonic tension controls body axis formation in avian embryos, Nature Communications **14**, 3266 (2023).

[38] G. Guglielmi, J. D. Barry, W. Huber, and S. De Renzis, An optogenetic method to modulate cell contractility during tissue morphogenesis, Developmental cell **35**, 646 (2015).

[39] E. Izquierdo, T. Quinkler, and S. De Renzis, Guided morphogenesis through optogenetic activation of rho signalling during early drosophila embryogenesis, Nature communications **9**, 2366 (2018).

[40] H. J. Gustafson, N. Claussen, S. De Renzis, and S. J. Streichan, Patterned mechanical feedback establishes a global myosin gradient, Nature Communications **13**, 7050 (2022).

[41] H. Guo, M. Swan, and B. He, Optogenetic inhibition of actomyosin reveals mechanical bistability of the mesoderm epithelium during drosophila mesoderm invagination, ELife **11**, e69082 (2022).

Supplementary material: Optimal Control of Short-Time Attractors in Active Nematics

Carlo Sinigaglia and Francesco Braghin
Politecnico di Milano, Department of Mechanical Engineering, 20156, Italy

Mattia Serra*
University of California San Diego, Department of Physics, CA 92093, USA
(Dated: April 24, 2024)

CONTENTS

S1. NOTATION

We adopt a slightly different notation than the main text to distinguish continuous functions and their associated numerical discretization. Continuous space-varying functions are denoted with lowercase bold arrowed symbols (i.e. $\vec{\mathbf{v}} \in H_0^1(\Omega)^2$) while their numerical discretization as the standard bold vector $\mathbf{v} \in \mathbb{R}^N$ where N is the number of degrees of freedom of the Finite Element discretization. Furthermore, matrices arising from the numerical discretization are denoted with uppercase letters i.e. $A \in \mathbb{R}^{N\times N}$.

S2. ANALYSIS OF THE STATE DYNAMICS

In order to set up the problem in the proper setting we need some basic notions from functional analysis, see e.g. [1]. We denote $L^2(\Omega)^2$ the space of vector-valued square integrable functions, that is $\{\vec{\mathbf{f}} | \int_\Omega \left\|\vec{\mathbf{f}}\right\|^2 d\Omega < \infty\}$ then, $H_0^1(\Omega)^2$ denotes the space of vector-valued square integrable functions with zero trace and square integrable gradient , that is $\{\vec{\mathbf{f}} \in L^2(\Omega)^2 \mid \int_\Omega \left\|\nabla\vec{\mathbf{f}}\right\|_F^2 < \infty \text{ and } \vec{\mathbf{f}}_{\partial\Omega} = \vec{\mathbf{0}}\}$ while $H^{-1}(\Omega)^2$ denotes its dual, that is the space of continuous linear functionals defined on $H_0^1(\Omega)^2$. We can now select the appropriate spaces for our problem. The state dynamics $\vec{\mathbf{v}} \in H_0^1(\Omega)^2$ while the control input $m \in H^1(\Omega)$. In this setting, the control operator can be defined as the linear operator $\mathbf{g} : H^1(\Omega) \mapsto H^{-1}(\Omega)^2$. The function $\vec{\mathbf{g}}(m) \in L^2(\Omega)^2$ since $m \in H^1(\Omega)$, as we will prove in the following theorem on the well-posedness of the state dynamics. The weak formulation of the state dynamics reads: find $\vec{\mathbf{v}} \in H_0^1(\Omega)^2$ such that

$$\int_\Omega \Big(-2p_1\Delta\vec{\mathbf{v}} - \nabla[\nabla\cdot\vec{\mathbf{v}}]\Big)\cdot\vec{\boldsymbol{\phi}}\, d\Omega = \int_\Omega \vec{\mathbf{g}}(m)\cdot\vec{\boldsymbol{\phi}}\, d\Omega$$

$\forall\vec{\boldsymbol{\phi}} \in H_0^1(\Omega)^2$, which can be rearranged in a more convenient form using integration by parts and homogeneous boundary conditions as

$$\int_\Omega 2p_1\nabla\vec{\mathbf{v}} : \nabla\vec{\boldsymbol{\phi}} + (\nabla\cdot\vec{\mathbf{v}})(\nabla\cdot\vec{\boldsymbol{\phi}})\, d\Omega = \int_\Omega -m\,\mathbf{A} : \nabla\vec{\boldsymbol{\phi}}\, d\Omega$$

$\forall\vec{\boldsymbol{\phi}} \in H_0^1(\Omega)^2$, where the operator : denotes the Frobenius innner product of two matrices, that is $\mathbf{A} : \mathbf{B} = \sum_i^n\sum_j^n A_{ij}B_{ij}$. Note that the Frobenius inner product induces a norm in the space of matrices that we denote as $\|\mathbf{A}\|_F := \sqrt{\mathbf{A} : \mathbf{A}}$, for more details, see e.g. [2]. Existence and uniqueness of solutions to this problem follow from an application of the Lax-Milgram lemma of functional analysis, see e.g. [1]. In particular, we can set the state problem in abstract form by defining the symmetric bilinear form $a(\vec{\mathbf{v}},\vec{\boldsymbol{\phi}}) := \int_\Omega 2p_1\nabla\vec{\mathbf{v}} : \nabla\vec{\boldsymbol{\phi}} + (\nabla\cdot\vec{\mathbf{v}})(\nabla\cdot\vec{\boldsymbol{\phi}})\, d\Omega$ and the linear functional $F_m\vec{\boldsymbol{\phi}} := \int_\Omega \vec{\mathbf{g}}(m)\cdot\vec{\boldsymbol{\phi}} d\Omega$. In this setting, we can prove the following result.

Proposition 1 *There exists a unique weak solution* $\vec{\mathbf{v}}$ *to*

$$a(\vec{\mathbf{v}},\vec{\boldsymbol{\phi}}) = F_m\vec{\boldsymbol{\phi}} \quad \forall\vec{\boldsymbol{\phi}} \in H_0^1(\Omega)^2.$$

Furthermore, $\vec{\mathbf{v}}$ depends continuously on the control function m that is

$$\|\vec{\mathbf{v}}\|_{H_0^1(\Omega)^2} \leq \frac{\sqrt{\alpha}C_p}{2p_1} \|m\|_{H^1(\Omega)^2}$$

where C_p is the Poincaré constant depending only on Ω and $\alpha = \max\{\|\nabla \cdot \mathbf{A}\|^2_{L^\infty(\Omega)}, \|\mathbf{A}\|^2_{L^\infty(\Omega)}\}$ does not depend on $\vec{\mathbf{v}}$ and m.

PROOF The control operator $\vec{\mathbf{g}}$ that appears on the right-hand side of the state equation can be bounded with respect to the H^1-norm of the control function m as

$$\begin{aligned}\|\vec{\mathbf{g}}\|^2_{L^2(\Omega)^2} &\leq \|(\nabla \cdot \mathbf{A})m\|^2_{L^2(\Omega)^2} + \|\mathbf{A}\nabla m\|^2_{L^2(\Omega)^2} \\ &\leq \|\nabla \cdot \mathbf{A}\|^2_{L^\infty(\Omega)} \|m\|^2_{L^2(\Omega)} + \|\mathbf{A}\|^2_{L^\infty(\Omega)} \|\nabla m\|^2_{L^2(\Omega)} \\ &\leq \alpha \|m\|^2_{H^1(\Omega)^2}\end{aligned}$$

where $\alpha = \max\{\|\nabla \cdot \mathbf{A}\|^2_{L^\infty(\Omega)}, M\}$. Note that we have used the triangle inequality and the operator bound on the matrix $\mathbf{A}$ which is assumed to be sufficiently smooth. Once this bound is established, we can prove existence and uniqueness of a weak solution to the state equation by showing that the hypotheses of Lax-Milgram lemma are satisfied, that is the bilinear form is continuous and coercive and the linear functional F_m is continuous with respect to the $H_0^1(\Omega)^2$-norm. Coerciveness can by proven as follows

$$\begin{aligned}a(\vec{\mathbf{v}}, \vec{\mathbf{v}}) &= \int_\Omega 2p_1 \nabla\vec{\mathbf{v}} : \nabla\vec{\mathbf{v}} + (\nabla \cdot \vec{\mathbf{v}})(\nabla \cdot \vec{\mathbf{v}})\, d\Omega \\ &\geq \int_\Omega 2p_1 \nabla\vec{\mathbf{v}} : \nabla\vec{\mathbf{v}} d\Omega = 2p_1 \|\vec{\mathbf{v}}\|^2_{H_0^1(\Omega)^2}\end{aligned}$$

since, thanks to Poincaré inequality, $\sqrt{\int_\Omega \nabla\vec{\mathbf{v}} : \nabla\vec{\mathbf{v}}\, d\Omega}$ is a norm in $H_0^1(\Omega)^2$. Continuity of the linear functional can be inferred by

$$\begin{aligned}|F_m\vec{\boldsymbol{\psi}}| &\leq \|\vec{\boldsymbol{g}}(m)\|_{L^2(\Omega)^2} \left\|\vec{\boldsymbol{\psi}}\right\|_{L^2(\Omega)^2} \\ &\leq \sqrt{\alpha}\, C_p \, \|m\|_{H^1(\Omega)^2} \left\|\vec{\boldsymbol{\psi}}\right\|_{H_0^1(\Omega)^2}\end{aligned}$$

using the bounds of the control operator $\vec{\mathbf{g}}$ with respect to the norm of m and the Poincarè inequality, i.e. $\left\|\vec{\boldsymbol{\psi}}\right\|_{L^2(\Omega)^2} \leq C_p \left\|\nabla\vec{\boldsymbol{\psi}}\right\|_{L^2(\Omega)^2} = C_p \left\|\vec{\boldsymbol{\psi}}\right\|_{H_0^1(\Omega)^2}$. Continuity of the state dynamics $\vec{\mathbf{v}}$ with respect to the control m is proven by plugging in $\vec{\mathbf{v}}$ as test function in the weak formulation of the problem and using the coercivity of the bilinear form. Indeed we have

$$2p_1 \|\vec{\mathbf{v}}\|^2_{H_0^1(\Omega)^2} \leq a(\vec{\mathbf{v}}, \vec{\mathbf{v}}) = F_m\vec{\mathbf{v}} \leq \sqrt{\alpha}C_p \|m\|_{H^1(\Omega)^2} \|\vec{\mathbf{v}}\|_{H_0^1(\Omega)^2}$$

from which we get

$$\|\vec{\mathbf{v}}\|_{H_0^1(\Omega)^2} \leq \frac{\sqrt{\alpha}C_p}{2p_1} \|m\|_{H^1(\Omega)^2}.$$

□

S3. ANALYSIS OF THE OPTIMAL CONTROL PROBLEM

We have already established existence and uniqueness of a solution to the state equation. It is left to prove that the functional J is weakly sequentially lower semicontinous. The term of the cost functional involving the control m is trivially weakly lower semicontinuous since it is the $H_1(\Omega)$-norm of the control function squared. We will now prove that the first term involving the eigenvalue s_1 is continuous in $\vec{\mathbf{v}}$ and thus weakly sequentially lower semicontinuous.

Before deriving a system of first-order necessary conditions for optimality we prove well-posedness by showing that $s_1 \in L^2(\Omega)$, indeed

$$\begin{aligned}\|s_1\|^2_{L^2(\Omega)} &= \int_\Omega s_1^2 d\Omega \leq \int_\Omega (s_1^2 + s_2^2) d\Omega \\ &\leq \int_\Omega \|\mathbf{S}(\vec{\mathbf{v}})\|^2_F \, d\Omega \qquad \text{(S1)} \\ &\leq \int_\Omega \|\nabla\vec{\mathbf{v}}\|^2_F \, d\Omega = \|\vec{\mathbf{v}}\|^2_{H_0^1(\Omega)^2} \qquad \text{(S2)}\end{aligned}$$

so that we have $\|s_1\|^2_{L^2(\Omega)} \leq \|\vec{\mathbf{v}}\|^2_{H_0^1(\Omega)^2}$, where we used the inequality $\sum_{i=1}^n s_i^2 \leq \|\mathbf{A}\|^2_F$ involving the eigenvalues of a matrix $\mathbf{A}$. The second inequality comes from the following reasoning, it holds that:

$$2\mathbf{S}(\vec{\mathbf{v}}) : \mathbf{S}(\vec{\mathbf{v}}) - \nabla\vec{\mathbf{v}} : \nabla\vec{\mathbf{v}} = \nabla \cdot (\nabla\vec{\mathbf{v}}\,\vec{\mathbf{v}} - (\nabla \cdot \vec{\mathbf{v}})\vec{\mathbf{v}}) + (\nabla \cdot \vec{\mathbf{v}})^2$$

Integrating over Ω and using the boundary conditions we get

$$\begin{aligned}\int_\Omega \|\mathbf{S}(\vec{\mathbf{v}})\|^2_F \, d\Omega &= \frac{1}{2}\Big(\int_\Omega \|\nabla\vec{\mathbf{v}}\|^2_F \, d\Omega + \int_\Omega (\nabla \cdot \vec{\mathbf{v}})^2 d\Omega\Big) \\ &\leq \int_\Omega \|\nabla\vec{\mathbf{v}}\|^2_F \, d\Omega \qquad \text{(S3)}\end{aligned}$$

since $(\nabla \cdot \vec{\mathbf{v}})^2 = (\mathrm{Tr}(\nabla\vec{\mathbf{v}}))^2 \leq \|\nabla\vec{\mathbf{v}}\|^2_F$.

We denote $J_s[\vec{\mathbf{v}}] := \int_\Omega (s_1 - z)^2 d\Omega$ and show that $|J_s[\vec{\mathbf{v}}_n] - J_s[\vec{\mathbf{v}}]| \to 0$ as $\vec{\mathbf{v}}_n \to \vec{\mathbf{v}}$. We also denote $s_{1,n} := s_1(\vec{\mathbf{v}}_n)$ and $s_1 := s_1(\vec{\mathbf{v}})$ to ease the notation. Note also that $J_s[\vec{\mathbf{v}}] = \int_\Omega (s_1 - z)^2 d\Omega = (s_1 - z, s_1 - z)_{L^2(\Omega)} = \|s_1 - z\|^2_{L^2(\Omega)}$ can be seen either as a scalar product in $L^2(\Omega)$ or as a tracking type cost functional involving the norm of $s_1 - z$, which is well-posed since $s_1 \in L^2(\Omega)$. Since we have $J_s[\vec{\mathbf{v}}_n] - J_s[\vec{\mathbf{v}}] = (s_{1,n} - z, s_{1,n} - z)_{L^2(\Omega)} -$

$(s_1 - z, s_1 - z)_{L^2(\Omega)}$, we can write

$$
\begin{aligned}
&(s_{1,n} - z, s_{1,n} - z)_{L^2(\Omega)} - (s_1 - z, s_1 - z)_{L^2(\Omega)} \\
&= (s_{1,n}, s_{1,n})_{L^2(\Omega)} - (s_1, s_1)_{L^2(\Omega)} \\
&-2(s_{1,n} - s_1, z)_{L^2(\Omega)} \pm (s_{1,n}, s_1)_{L^2(\Omega)} \\
&= (s_{1,n}, s_{1,n} - s_1)_{L^2(\Omega)} + (s_1, s_{1,n} - s_1) - 2(s_{1,n} - s_1, z) \\
&\leq \|s_{1,n}\|_{L^2(\Omega)} \|s_{1,n} - s_1\|_{L^2(\Omega)} \\
&+ \|s_1\|_{L^2(\Omega)} \|s_{1,n} - s_1\|_{L^2(\Omega)} + 2\|z\|_{L^2(\Omega)} \|s_{1,n} - s_1\|_{L^2(\Omega)} \\
&= \Big(\|s_{1,n}\|_{L^2(\Omega)} + \|s_1\|_{L^2(\Omega)} + 2\|z\|_{L^2(\Omega)} \Big) \|s_{1,n} - s_1\|_{L^2(\Omega)} \\
&= C \|s_{1,n} - s_1\|_{L^2(\Omega)}
\end{aligned} \tag{S4}
$$

so that finally we have $J_s[\vec{\mathbf{v}}_n] - J_s[\vec{\mathbf{v}}] \leq C\|s_{1,n} - s_1\|_{L^2(\Omega)}$, where we have used the properties of the inner product and the Cauchy-Schwarz inequality in $L^2(\Omega)$. Note that the constant $C := \Big(\|s_{1,n}\| + \|s_1\| + 2\|z\| \Big)$ is well-defined and finite since $s_{1,n}, s_1, z \in L^2(\Omega)$. Now, if we can prove that $\|s_{1,n} - s_1\|_{L^2(\Omega)} \leq L\|\vec{\mathbf{v}}_n - \vec{\mathbf{v}}\|_{H_0^1(\Omega)^2}$ for some constant $L > 0$,the result follows. In proving that this indeed holds we need a theorem from eigenvalues perturbation analysis from [2], Chapter 6, Corollary 6.3.8 that we state here. If $\mathbf{A}$ and $\mathbf{E}$ are symmetric matrices, denoting $\hat{s}$ the eigenvalues of $\mathbf{A} + \mathbf{E}$ and by s the eigenvalues of $\mathbf{A}$ it holds that $\sum_{i=1}^n |\hat{s}_i - s_i|^2 \leq \|\mathbf{E}\|_F^2$. We can write

$$
\begin{aligned}
\|s_{1,n} - s_1\|_{L^2(\Omega)}^2 &= \int_\Omega (s_{1,n} - s_1)^2 d\Omega \\
&\leq \int_\Omega \|\mathbf{S}(\vec{\mathbf{v}}_n) - \mathbf{S}(\vec{\mathbf{v}})\|_F^2 \, d\Omega \\
&= \int_\Omega \|\mathbf{S}(\vec{\mathbf{v}}_n - \vec{\mathbf{v}})\|_F^2 \, d\Omega \\
&\leq \int_\Omega \|\nabla(\vec{\mathbf{v}}_n - \vec{\mathbf{v}})\|_F^2 \, d\Omega = \|\vec{\mathbf{v}}_n - \vec{\mathbf{v}}\|_{H_0^1(\Omega)^2}^2
\end{aligned} \tag{S5}
$$

where in applying Corollary 6.3.8 we set $\mathbf{A} = \mathbf{S}(\vec{\mathbf{v}}(\mathbf{x}))$ and $\mathbf{E} = \mathbf{S}(\vec{\mathbf{v}}_n(\mathbf{x})) - \mathbf{S}(\vec{\mathbf{v}}(\mathbf{x}))$ which are both symmetric.

S4. DERIVATION OF THE OPTIMALITY SYSTEM

The Gateaux derivative of $\mathcal{L}$ computed at $\vec{\mathbf{v}}$ in the direction $\vec{\boldsymbol{\psi}}$ can be written as:

$$
\begin{aligned}
\mathcal{L}'(\vec{\mathbf{v}})\vec{\boldsymbol{\psi}} &= \frac{\partial}{\partial\epsilon}\Big|_{\epsilon=0} \Big(\frac{1}{2} \int_\Omega (s_1(\mathbf{S}(\vec{\mathbf{v}} + \epsilon\vec{\boldsymbol{\psi}})) - z)^2 \, d\Omega \\
&+ \int_\Omega \vec{\boldsymbol{\lambda}} \cdot \Big(2p_1 \Delta(\vec{\mathbf{v}} + \epsilon\vec{\boldsymbol{\psi}}) + \nabla[\nabla \cdot (\vec{\mathbf{v}} + \epsilon\vec{\boldsymbol{\psi}})] \Big) \, d\Omega \Big).
\end{aligned} \tag{S6}
$$

In the following we will need the differentiation formula for a non repeated eigenvalue λ with respect to a symmetric matrix function $\mathbf{A}(\epsilon)$ parametrized with respect to a scalar $\epsilon \in \mathbb{R}$, see e.g. [2], Theorem 6.3.12, Chapter 6. Indeed, we have $\frac{d\lambda}{d\epsilon}\Big|_{\epsilon=\epsilon_0} = \vec{\boldsymbol{\xi}}(\epsilon_0)^\top \frac{d\mathbf{A}}{d\epsilon}\Big|_{\epsilon=\epsilon_0} \vec{\boldsymbol{\xi}}(\epsilon_0)$ where $\vec{\boldsymbol{\xi}}$ is the associated normalized eigenvector.

The first term in (S6) can be rearranged using integration by parts and the linearity of Frobenius inner product as

$$
\begin{aligned}
&\frac{\partial}{\partial\epsilon}\Big|_{\epsilon=0} \Big(\frac{1}{2} \int_\Omega (s_1(\mathbf{S}(\vec{\mathbf{v}} + \epsilon\vec{\boldsymbol{\psi}})) - z)^2 \, d\Omega \\
&= \int_\Omega (s_1(\mathbf{S}(\vec{\mathbf{v}})) - z) \frac{\partial}{\partial\epsilon}\Big|_{\epsilon=0} s_1(\mathbf{S}(\vec{\mathbf{v}} + \epsilon\vec{\boldsymbol{\psi}}) \, d\Omega \\
&= \int_\Omega (s_1 - z) \, \vec{\boldsymbol{\xi}}_1^\top \vec{\mathbf{S}}(\vec{\boldsymbol{\psi}}) \vec{\boldsymbol{\xi}}_1 d\Omega = \int_\Omega (s_1 - z) \, \vec{\boldsymbol{\xi}}_1 \otimes \vec{\boldsymbol{\xi}}_1 : \mathbf{S}(\vec{\boldsymbol{\psi}}) d\Omega \\
&= -\int_\Omega \nabla \cdot \Big((s_1 - z) \, \vec{\boldsymbol{\xi}}_1 \otimes \vec{\boldsymbol{\xi}}_1 \Big) \cdot \vec{\boldsymbol{\psi}} d\Omega \\
&+ \int_\Omega \nabla \cdot ((s_1 - z) \, \vec{\boldsymbol{\xi}}_1 \otimes \vec{\boldsymbol{\xi}}_1 \vec{\boldsymbol{\psi}}) d\Omega \\
&= -\int_\Omega \nabla \cdot \Big((s_1 - z) \, \vec{\boldsymbol{\xi}}_1 \otimes \vec{\boldsymbol{\xi}}_1 \Big) \cdot \vec{\boldsymbol{\psi}} d\Omega \\
&+ \cancel{\int_{\partial\Omega} ((s_1 - z) \, \vec{\boldsymbol{\xi}}_1 \otimes \vec{\boldsymbol{\xi}}_1 \vec{\boldsymbol{\psi}}) d\Omega}
\end{aligned}
$$

where we have used the fact that for a matrix-valued function $\mathbf{A}(\mathbf{x})$ and a vector-valued function $\vec{\boldsymbol{\psi}}(\mathbf{x})$ it holds that $\nabla \cdot (\mathbf{A}\vec{\boldsymbol{\psi}}) = (\nabla \cdot \mathbf{A}) \cdot \vec{\boldsymbol{\psi}} + \mathbf{A} : \nabla\vec{\boldsymbol{\psi}}$. Using integration by parts, the second term of Equation (S6) reads:

$$
\begin{aligned}
&\frac{\partial}{\partial\epsilon}\Big|_{\epsilon=0} \int_\Omega \vec{\boldsymbol{\lambda}} \cdot \Big(2p_1 \Delta(\vec{\mathbf{v}} + \epsilon\vec{\boldsymbol{\psi}}) + \nabla[\nabla \cdot (\vec{\mathbf{v}} + \epsilon\vec{\boldsymbol{\psi}})] \Big) \, d\Omega \Big) \\
&= \int_\Omega \Big(2p_1 \Delta\vec{\boldsymbol{\lambda}} + \nabla[\nabla \cdot \vec{\boldsymbol{\lambda}}] \Big) \cdot \vec{\boldsymbol{\psi}} \, d\Omega.
\end{aligned} \tag{S7}
$$

From the optimality condition

$$
\mathcal{L}'(\vec{\mathbf{v}})\vec{\boldsymbol{\psi}} = 0 \quad \forall \vec{\boldsymbol{\psi}} \in H_0^1(\Omega)
$$

we obtain the strong form of the adjoint equation which is a linear elliptic PDE of the form

$$
\begin{aligned}
&-2p_1 \Delta\vec{\boldsymbol{\lambda}} - \nabla[\nabla \cdot \vec{\boldsymbol{\lambda}}] = -\nabla \cdot \Big((s_1 - z) \, \vec{\boldsymbol{\xi}}_1 \otimes \vec{\boldsymbol{\xi}}_1 \Big) \quad \text{in} \quad \Omega \\
&\vec{\boldsymbol{\lambda}} = \vec{\mathbf{0}} \qquad\qquad\qquad\qquad\qquad\qquad\qquad\qquad\quad \text{on} \quad \partial\Omega
\end{aligned}
$$

where $\vec{\boldsymbol{\xi}}_1(\mathbf{x})$ is the space varying eigenvector associated to the minimum eigenvalue $s_1(\mathbf{x})$ and $\vec{\boldsymbol{\lambda}}(\mathbf{x})$ is the adjoint variable. The Euler equation can be recovered by taking the first variation of the Lagrangian with respect to the control function m.

$$
\mathcal{L}'(m)h = \beta \Big(\int_\Omega m \, h + \nabla m \cdot \nabla h \, d\Omega \Big) + \frac{\partial}{\partial\epsilon}\Big|_0 \int_\Omega \vec{\boldsymbol{\lambda}} \cdot \vec{\mathbf{g}}(m + \epsilon h) \, d\Omega.
$$

Due to the linearity of the inner product and of $\vec{\mathbf{g}}$ we have:

$$
\begin{aligned}
&\frac{\partial}{\partial\epsilon}\Big|_0 \int_\Omega \vec{\boldsymbol{\lambda}} \cdot \vec{\mathbf{g}}(m + \epsilon h) \, d\Omega = \frac{\partial}{\partial\epsilon}\Big|_0 \int_\Omega \boldsymbol{\lambda} \cdot \Big(\vec{\mathbf{g}}(m) + \epsilon\vec{\mathbf{g}}(h) \Big) \, d\Omega \\
&= \int_\Omega \vec{\boldsymbol{\lambda}} \cdot \vec{\mathbf{g}}(h) d\Omega.
\end{aligned}
$$

Using integration by parts and the explicit form of $\vec{\mathbf{g}}$ we get:

$$\int_\Omega \vec{\boldsymbol{\lambda}} \cdot \vec{\mathbf{g}}(h) d\Omega = \int_\Omega \vec{\boldsymbol{\lambda}} \cdot \nabla \cdot \Big(\mathbf{A} h\Big) d\Omega = -\int_\Omega \nabla \vec{\boldsymbol{\lambda}} : \mathbf{A}\, h\, d\Omega$$

since $\vec{\boldsymbol{\lambda}}$ should satisfy homogeneous Dirichlet boundary conditions. The Euler equation is obtained by the optimality condition:

$$\mathcal{L}'(m)h = 0 \quad \forall h \in H^1(\Omega)$$

which gives

$$-\beta \Delta m + \beta m - \nabla \vec{\boldsymbol{\lambda}} : \mathbf{A} = 0.$$

S5. NUMERICAL IMPLEMENTATION

We select linear piecewise continuous finite elements and use the software package `deal.II` [3] for the finite element approximation while `NLopt` [4] is used for the gradient-based optimization. The discretized system of optimality conditions read

$$\begin{aligned} A\mathbf{v} &= B\mathbf{m} + \mathbf{d} \\ A\boldsymbol{\lambda} &= \mathbf{f}(\mathbf{v}) \\ \beta(A_m + M)\mathbf{m} + B^\top \boldsymbol{\lambda} &= \mathbf{0} \end{aligned}$$

where A and M are the standard stiffness and mass matrix of the Finite Element formulation of vector-valued and scalar-valued elliptic problems, respectively. The discretized input operator is $B_{ij} = -\int_\Omega \nabla \vec{\boldsymbol{\psi}}_i : \mathbf{A}\, \psi_j\, d\Omega$ where $\vec{\boldsymbol{\psi}}_i$ and ψ_j are the associated vector and scalar basis functions, respectively. The nonlinear forcing in the adjoint equation is obtained from the weak formulation of the adjoint equation as $\mathbf{f}_i = \int_\Omega (s_1 - z)\, \vec{\boldsymbol{\xi}}_1 \otimes \vec{\boldsymbol{\xi}}_1 : \mathbf{S}(\vec{\boldsymbol{\psi}}_i) d\Omega$ where $s_1(\mathbf{v})$ and $\vec{\boldsymbol{\xi}}_1(\mathbf{v})$ are obtained from the numerical solution of $\mathbf{v}$. At each iteration of the gradient-based optimizer the reduced gradient can be computed by solving state and adjoint equation, then we have $\nabla J = \beta(A_m + M)\mathbf{m} + B^\top \boldsymbol{\lambda}$ which is used for the control update. Where not otherwise stated, the optimization is completed when the L^2 norm of the reduced gradient is less than 10^{-7}.

S6. OBJECTIVITY

Assume $\mathbf{v}(\mathbf{x}, t)$ is the velocity field solving the OCP (eq. (2)) or one experimentally measured as in Figs. 1a-b. Objectivity is a fundamental axiom of mechanics [5] that states that the material response of a deforming continuum is independent of the reference frame chosen to describe the motion, for all frames related by Euclidean (or distance preserving) transformations of the form: $\tilde{\mathbf{x}} = \mathbf{Q}(t)\mathbf{x} + \mathbf{b}(t)$, where $\mathbf{Q}(t) \in SO(2)$ and $\mathbf{b}(t)$ is a translation vector. Therefore, the location of short-time attractors, which is related to fluid deformation and motion, cannot depend on the reference frame choice.

Denoting by $\tilde{(\cdot)}$ and $(\cdot)$ the same quantity expressed in the $\tilde{\mathbf{x}}$ and $\mathbf{x}$ frames, scalar objective quantities must transform [5] as $\tilde{c}(\tilde{\mathbf{x}}, t) = c(\mathbf{x}, t)$, objective vector fields must transform as $\tilde{\mathbf{c}}(\tilde{\mathbf{x}}, t) = \mathbf{Q}(t)\mathbf{c}(\mathbf{x}, t)$, etc.. Short-time attractors are objective because $\tilde{s}_1(\tilde{\mathbf{x}}, t) = s_1(\mathbf{x}, t)$ [6]. By contrast, it is well known that the velocity field and its streamlines are not as

$$\tilde{\mathbf{v}}(\tilde{\mathbf{x}}, t) = \mathbf{Q}(t)\mathbf{v}(\mathbf{Q}^\top \tilde{\mathbf{x}}, t) + \dot{\mathbf{Q}}(t)\mathbf{Q}^\top(t)\tilde{\mathbf{x}} + \dot{\mathbf{b}}(t). \quad \text{(S7)}$$

To visualize the effects of frame invariance, we solve the OCP in eqs. (1-2) from the main text, setting for simplicity $\mathbf{d} = \mathbf{0}$, and z_1 in order to create a short-term attractor along the positive $y-$axis (Figs. S1a-b). We then select a coordinate frame $\tilde{\mathbf{x}}$ with $\dot{\mathbf{b}} = \mathbf{0}$ and constant angular velocity ω so that

$$\mathbf{Q}(t) = \begin{bmatrix} \cos(\omega t) & -\sin(\omega t) \\ \sin(\omega t) & \cos(\omega t) \end{bmatrix}, \quad \dot{\mathbf{Q}}(t) = \omega \begin{bmatrix} -\sin(\omega t) & -\cos(\omega t) \\ \cos(\omega t) & -\sin(\omega t) \end{bmatrix}. \quad \text{(S8)}$$

The frame rotation does not affect s_1 and the location of material attraction, but distorts the streamlines of $\tilde{\mathbf{v}}$ as shown in Figure S1c, highlighting the fact that the streamlines or the velocity field are suboptimal to identify material attraction. Using the same coordinate transformation, a similar conclusion holds using the experimental velocity field used in Fig.1, as shown in Fig. S2.

S7. SENSITIVITY ANALYSIS

S7.1 Sensitivity to p_0 and space-dependent cable orientation

To show the generality of our method to any attractor configuration, here we consider a circular target shape shown in Fig S4 left. We note that increasing p_0 increases the control authority, and $p_0 = 1$ is the "least" controllable case because the isotropic active stress vanishes (see eq. (1)). We select this worst-case scenario to study the effect of space-varying cable orientation. In this case, the control operator is $\mathbf{g}(m) = \nabla \cdot (\mathbf{A}m)$ where $\mathbf{A} = 2p_1\mathbf{B}(\phi)$. Figures S3 show the effect of space-varying cable orientation ϕ with minimal control authority $p_0 = 1$. We consider three types of space-dependent $\phi(\mathbf{x})$, and show the coorresponding results in separate columns. In the first column, $\phi(\mathbf{x})$ varies continuosly in space from $-1[rad]$ to $1[rad]$ according to the function $\phi(\mathbf{x}) = \sin(\pi x)\cos(\pi y)$. The second and third cases consider a radial and tangential orientation, respectively.

Figures S3 show two important results. First, our control problem is able to create short-term attractors that

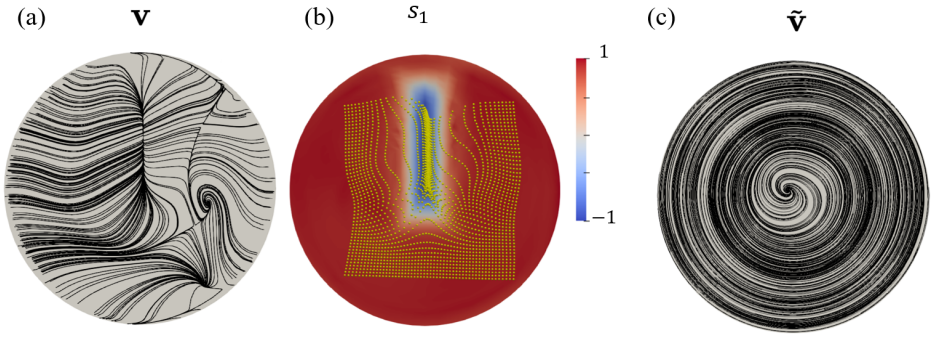

FIG. S1. Solution of the OCP in eqs. (1-2) from the main text, setting $\mathbf{d} = \mathbf{0}$ and z_1 to create a short-term attractor along the positive $y-$axis. (a) Streamlines of the velocity field $\mathbf{v}$. (b) $s_1(\mathbf{x})$ marks short-time attraction, confirmed by fluid tracers advected by $\mathbf{v}$ over a short time, as Figs. 1,2,4. (c) Streamlines of the velocity field $\tilde{\mathbf{v}}$. The tilde frame is rotating with respect to the standard frame at constant angular velocity $\omega = 120\ rad$ (time is in nondimensional units). The rotated frame is displayed at the time when it is instantaneously aligned with the standard frame. While $\mathbf{v}$ and the streamlines are frame-dependent, $s_1(\mathbf{x}) = \tilde{s}_1(\tilde{\mathbf{x}})$ is not, correctly predicting short-term attractors regardless of the arbitrary choice of the reference frame used to describe motion.

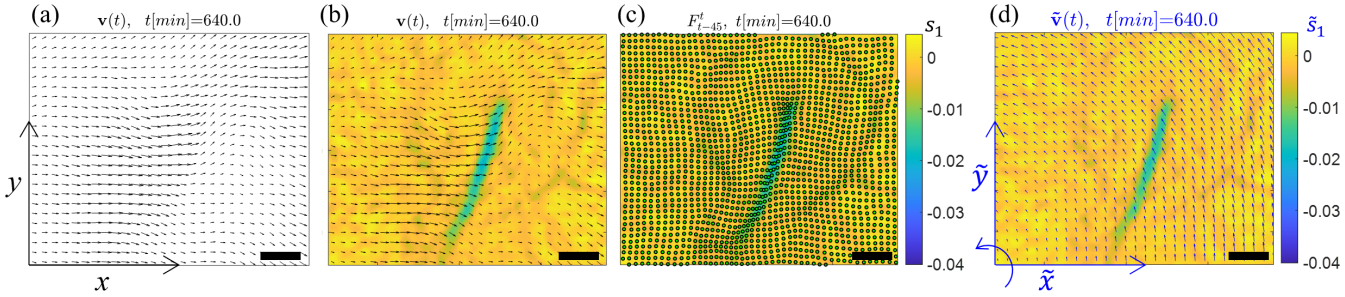

FIG. S2. Same as Figs. 1a-b for a different time. (a) Velocity field $\mathbf{v}(\mathbf{x})$. (b) $\mathbf{v}(\mathbf{x})$ and $s_1(\mathbf{x})$ field. (c) $s_1(\mathbf{x})$ locates a short-term attractor, as verified by fluid tracers (green) advected by $\mathbf{v}(\mathbf{x})$ over a short time from uniform initial conditions, as in Figs. 1b. (d) Velocity field $\tilde{\mathbf{v}}(\tilde{\mathbf{x}})$ obtained from eqs. (S7,S8), setting $\omega = 1\ rad/min$, $\dot{\mathbf{b}} = \mathbf{0}$ and starting with $\tilde{\mathbf{x}}$ and $\mathbf{x}$ aligned at the time shown $t = 640$. $\mathbf{v}(\mathbf{x})$ and its streamlines are frame dependent and hence are strongly affected by the choice (motion) of the reference frame. By contrast, $s_1(\mathbf{x}) = \tilde{s}_1(\tilde{\mathbf{x}})$ is objective and predicts the correct location of short-term attractors.

are very close to the target (compare the last row of Figure S3 with the circular target shown in Figure S4 left) even in the worst-case setting ($p_0 = 1$). In the case of radial ϕ distribution (mid-column) the target eigenvalue shape is reached with minimal control effort, as shown by the magnitude of $\mathbf{g}(m)$. Second, as noticed in Fig. 1 and discussed in the main text, comparing rows two and five shows that attractors remain hidden to inspection of the velocity field $\mathbf{v}$. Using $p_0 = 2$ (80% reduction compared to main text) and tangential cable configurations, our optimal control framework easily reaches the desired target, as shown in Fig. S4.

S7.2 Sensitivity to β

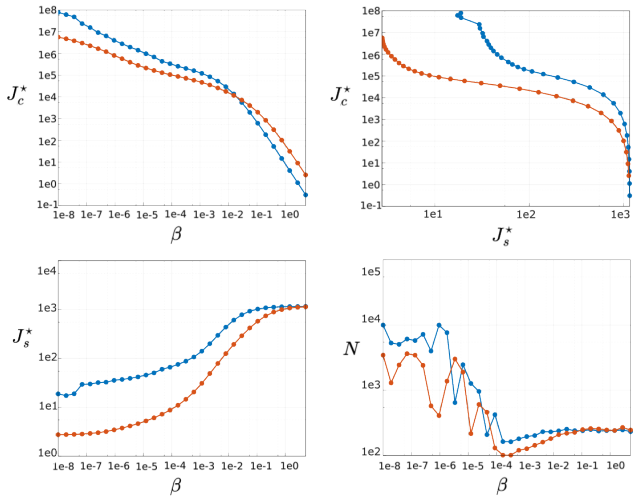

FIG. S6. $J_c^\star$ optimal control cost, $J_s^\star$ optimal state cost, N number of iterations of LM-BFGS. Number of dof for these simulations 3939 (2626 state +1313 control). $p_0 = 1$ is in blue while $p_0 = 10$ in orange.

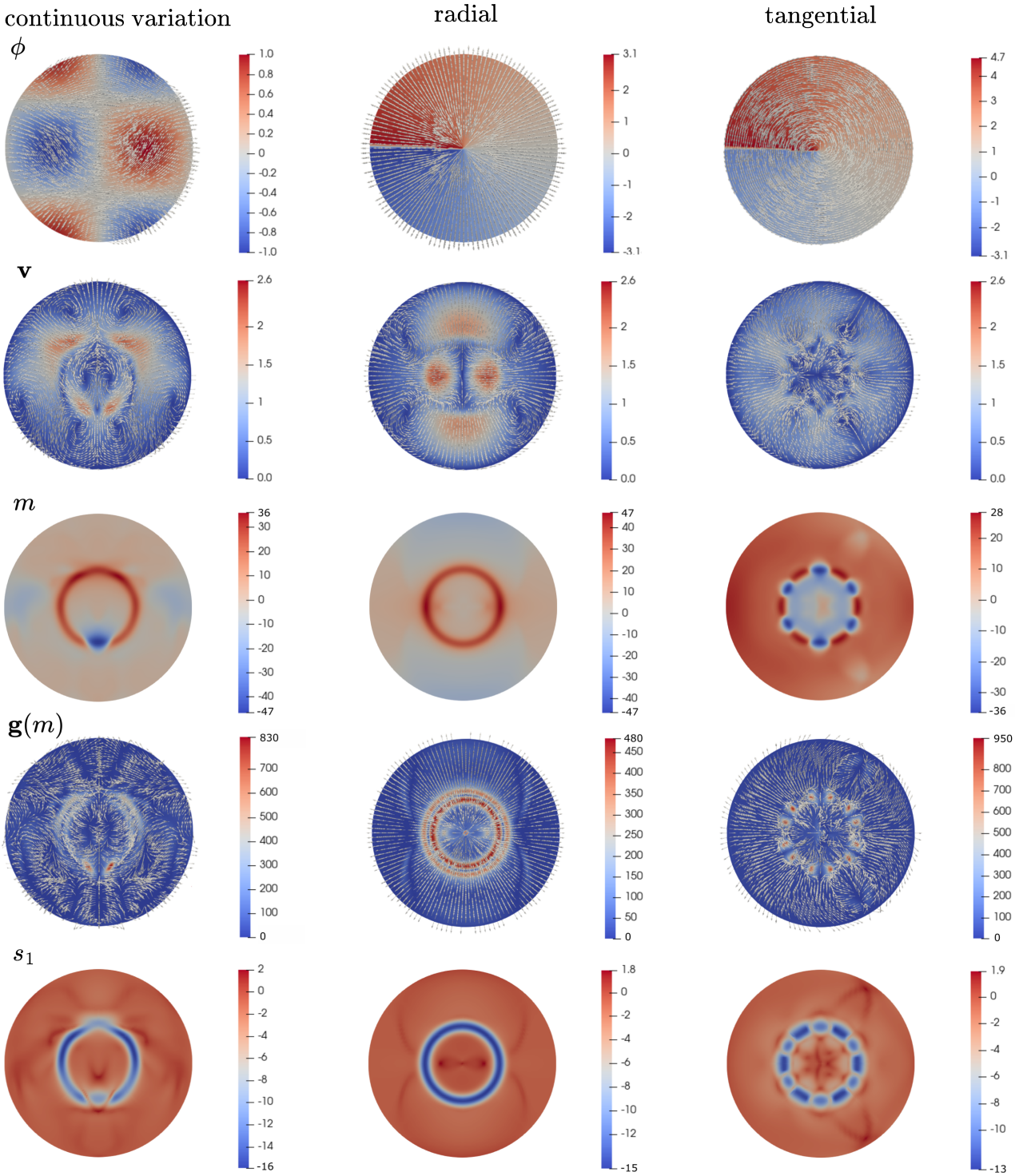

FIG. S3. Effect of spatially inhomogeneous cable orientation ϕ. Each column corresponds to different $\phi(\mathbf{x})$ (first row), visualized as a scalar field as well as a direction field $\mathbf{e}_\phi(\mathbf{x}) = (\cos(\phi(\mathbf{x})), \sin(\phi(\mathbf{x})))$. The first column corresponds to a continuous variation of ϕ, while the second and third columns correspond to radial and tangential $\phi(\mathbf{x})$. Different raws show the corresponding optimal velocity field $\mathbf{v}$, control action m, active forces $\mathbf{g}(m)$ and minimum eigenvalue s_1.

First, we study the effect of the control weighting β for the rectangular-shaped target discussed in the main text. Without loss of generality, we set the disturbance $\mathbf{d}$ to zero, and split the cost functional into state cost $J_s = \int_\Omega (s_1 - z)^2 \, d\Omega$ and control cost $J_c = \int_\Omega \left(m^2 + \|\nabla m\|^2 \right) d\Omega$, so that the overall functional is

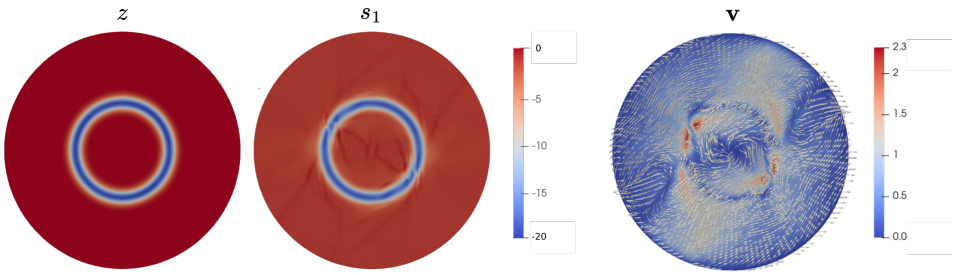

FIG. S4. Optimal control results for a circular target attractor, $p_0 = 2$, and tangential cable configurations. From left to right: eigenvalue target, minimum eigenvalue achieved and velocity field.

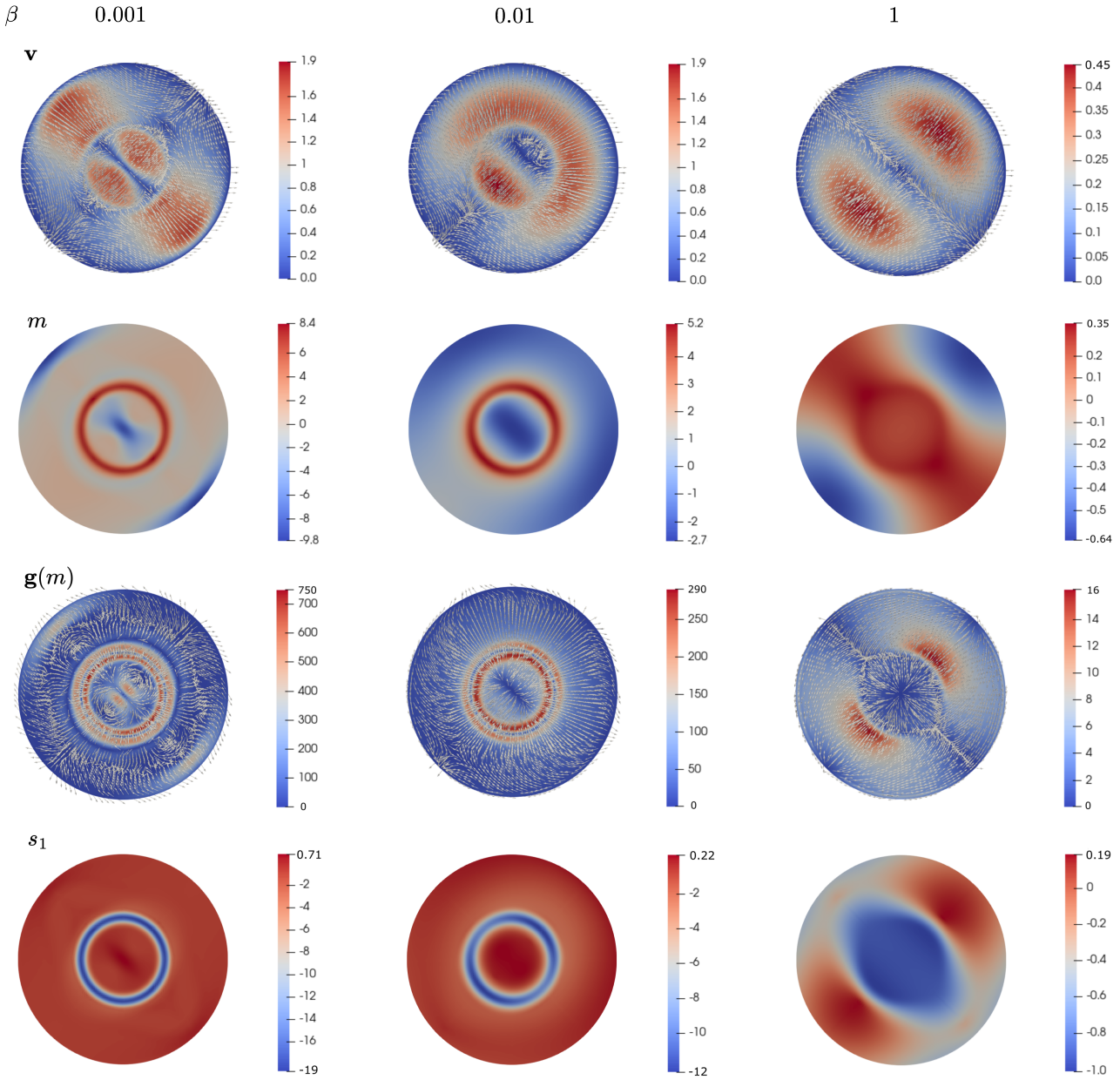

FIG. S5. Optimal patterns of velocity field $\mathbf{v}$, control action m, active forces $\mathbf{g}(m)$ and minimum eigenvalue s_1 for control weigths parameters $\beta = 0.001, 0.01, 1$ ordered per columns. $p_0 = 1$ and $\phi = \frac{\pi}{4}$ constant.

$J = J_s + \beta J_c$. As β is reduced, higher importance is given to reaching the target, i.e., minimizing J_s. However, a small β entails a highly irregular control, taking more iterations to converge within a given tolerance. Figure S6 shows a parametric study of the optimal state cost $J_s^\star$, the optimal control cost $J_c^\star$ and the number of iterations needed to converge N as a function of the control weighting parameter β. The setup with $p_0 = 1$ in blue takes more iterations to converge and asymptotically reaches a higher state cost when decreasing β. This is due to the structure of the control operator $\mathbf{g}(m) = \mathbf{g} = p_1[2(\mathbf{B}\nabla m + m\nabla\cdot\mathbf{B}) + (p_0-1)\nabla m]$ which for $p_0 = 1$ cancels out the contribution independent of $\mathbf{B}(\phi)$. The setup considered in the main text with $p_0 = 10$ is shown in orange.

Next, we study the effect of β for the case of circular target attractor shown in Fig S4 left and constant cable orientation set at $\frac{\pi}{4}$. Figure S5 shows the optimal control results for this configuration and increasing values of β corresponding to different columns. As expected, the largest β significantly penalizes the control cost and prevents achieving the desired target.

S7.3 Sensitivity to the disturbance force

The sensitivity of the optimal cost functional to perturbation of the disturbance around a nominal value can be deduced from the adjoint field [7]. To better illustrate this concept, consider the discrete Lagrangian of the problem

$$\begin{aligned}\mathcal{L}_d = &\frac{1}{2}(\mathbf{s}_1(\mathbf{v}) - \mathbf{z})^\top M(\mathbf{s}_1(\mathbf{v}) - \mathbf{z}) \\ &+ \frac{\beta}{2}\mathbf{m}^\top(A_m + M)(\mathbf{m}) \\ &+ \boldsymbol{\lambda}^\top\Big(B\mathbf{m} + \mathbf{d} - A\mathbf{v}\Big),\end{aligned}$$

where $\mathbf{m}$,$\mathbf{v}$,$\mathbf{d}$ and $\boldsymbol{\lambda}$ are the finite element discretization of the control, velocity, disturbance and adjoint field, respectively (see Section S5). $\mathbf{s}_1$ is a nonlinear function that maps the finite element velocity field $\mathbf{v}$ to the discrete representation of the minimal eigenvalue field s_1. Furthermore note that $\frac{\partial}{\partial \mathbf{v}}\frac{1}{2}(\mathbf{s}_1(\mathbf{v})-\mathbf{z})^\top M(\mathbf{s}_1(\mathbf{v})-\mathbf{z}) = \mathbf{f}(\mathbf{v})$, as defined in Secion S5. The optimal discretized cost functional can be parametrized by the disturbance $\mathbf{d}$ as

$$\begin{aligned}J_d^\star(\mathbf{d}) = &\min_{\mathbf{v},\mathbf{m}} \frac{(\mathbf{s}_1(\mathbf{v})-\mathbf{z})^\top M(\mathbf{s}_1(\mathbf{v})-\mathbf{z}) + \beta\mathbf{m}^\top(A_m+M)(\mathbf{m})}{2} \\ &s.t. \quad A\mathbf{v} = B\mathbf{m} + \mathbf{d}.\end{aligned}$$

Since at optimality, the constraints are satisfied together with the first-order necessary optimality conditions described in Section S5, it follows that

$$\begin{aligned}&\frac{dJ_d^\star(\mathbf{d})}{d\mathbf{d}} = \frac{d\mathcal{L}_d^\star(\mathbf{d})}{d\mathbf{d}} = (\mathbf{s}_1(\mathbf{v}) - \mathbf{z})^\top M\frac{\partial \mathbf{s}_1}{\partial \mathbf{v}}\frac{\partial \mathbf{v}}{\partial \mathbf{d}} \\ &+ \beta\mathbf{m}^\top(A_m + M)\frac{\partial \mathbf{m}}{\partial \mathbf{d}} + \boldsymbol{\lambda}^\top B\frac{\partial \mathbf{m}}{\partial \mathbf{d}} - \boldsymbol{\lambda}^\top A\frac{\partial \mathbf{v}}{\partial \mathbf{d}} \\ &+ \frac{\partial \boldsymbol{\lambda}}{\partial \mathbf{d}}^\top(B\mathbf{m} + \mathbf{d} - A\mathbf{v}) + \boldsymbol{\lambda}^\top \\ &= \cancel{\Big((\mathbf{s}_1(\mathbf{v}) - \mathbf{z})^\top M\frac{\partial \mathbf{s}_1}{\partial \mathbf{v}} - \boldsymbol{\lambda}^\top A\Big)\frac{\partial \mathbf{v}}{\partial \mathbf{d}}} \\ &+ \cancel{(\beta\mathbf{m}^\top(A_m + M) + \boldsymbol{\lambda}^\top B)\frac{\partial \mathbf{m}}{\partial \mathbf{d}}} + \frac{\partial \boldsymbol{\lambda}}{\partial \mathbf{d}}^\top \cancel{(B\mathbf{m} + \mathbf{d} - A\mathbf{v})} + \boldsymbol{\lambda}^\top.\end{aligned}$$

Therefore, we have $\frac{dJ_d^\star(\mathbf{d})}{d\mathbf{d}} = \boldsymbol{\lambda}^\top$, that is, the sensitivity of the optimal value of the cost functional to the disturbance is simply the optimal adjoint field. The first order expansion of the optimal cost functional is $J^\star(\mathbf{d} + \delta\mathbf{d}) \approx J^\star(\mathbf{d}) + \boldsymbol{\lambda}^\top\delta\mathbf{d}$ where $\delta\mathbf{d}$ is a perturbation of the disturbance from a nominal value.

Figure S7 shows the sensitivity for different target shapes (rows): circular (as in Fig S4 left) or rectangular (as in Fig 2), and cable orientation (columns) as in Fig. S3, together with the associated optimal cost $J^\star$. Because we observed that changing the nominal value of the disturbance does not fundamentally change the sensitivity field, we set it to zero in all cases. As in the earlier sections, we show the results of our sensitivity analysis in the worst-case scenario corresponding to the minimal control authority, i.e., $\beta = 10^{-4}$, $p_0 = 1$. In the case of circular target and radial ϕ, the most sensitive region is around the target shape, while in the cases of rectangular target with radial and tangential ϕ, we notice that the direction of the sensitivity is roughly orthogonal to the direction of the cable orientation. This, in turn, implies that in the worst-case setting of $p_0 = 1$, a disturbance can affect the optimal cost the most if it is orthogonal to the cable orientation. Finally, we show in Figure S8 the result of the same control problem discussed in the main text for the case of a random disturbance field both in amplitude and orientation.

S8. ALGORITHMIC SUMMARY AND APPLICATION TO AVIAN MORPHOGENESIS

Here, we summarize the steps required to apply our optimal control algorithm (Eq. 3).

- Identify the imposed (or disturbance) force $\mathbf{d}(\mathbf{x})$,
- identify the boundary condition of the problem,
- specify the desired short-time attractor configuration $z(\mathbf{x})$,
- solve Eq. 3 and compute the optimal $m^*(\mathbf{x})$.

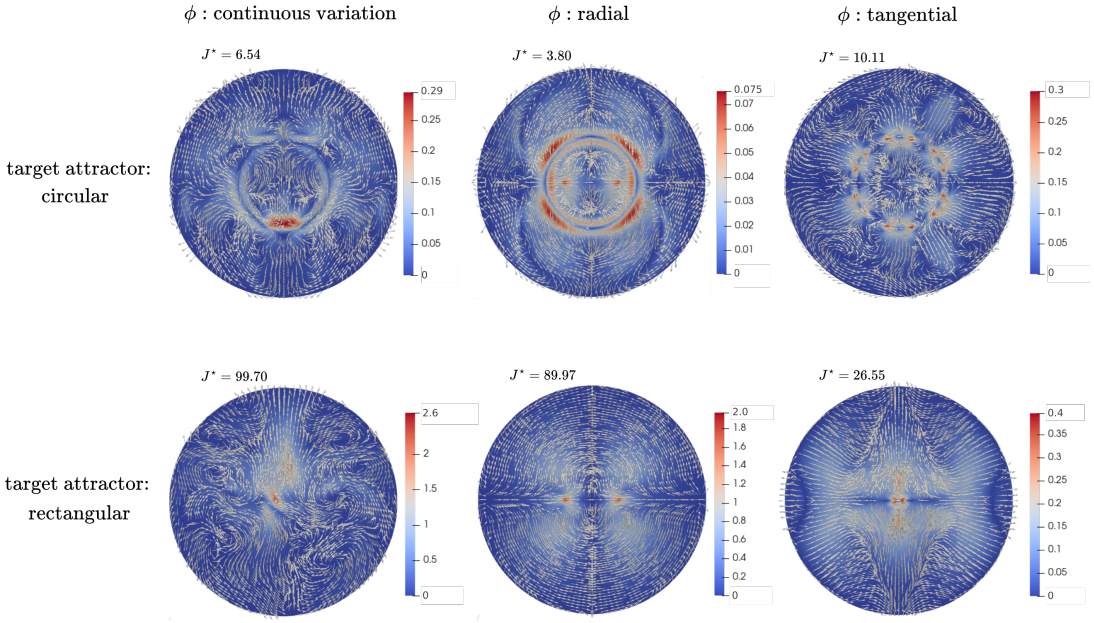

FIG. S7. Sensitivity to the disturbance force for different ϕ and target attractor geometries. Adjoint fields $\boldsymbol{\lambda}$ for circular (Fig S4 left) and rectangular (Fig 2) target shapes ordered by rows, and for different configurations of cable orientation ϕ ordered by columns as in Fig. S3. The adjoint represents the sensitivity of the optimal cost with respect to disturbance perturbations, i.e. $\frac{dJ^\star(\mathbf{d})}{d\mathbf{d}} = \boldsymbol{\lambda}^\top$. $J^\star$ quantifies the corresponding optimal cost.

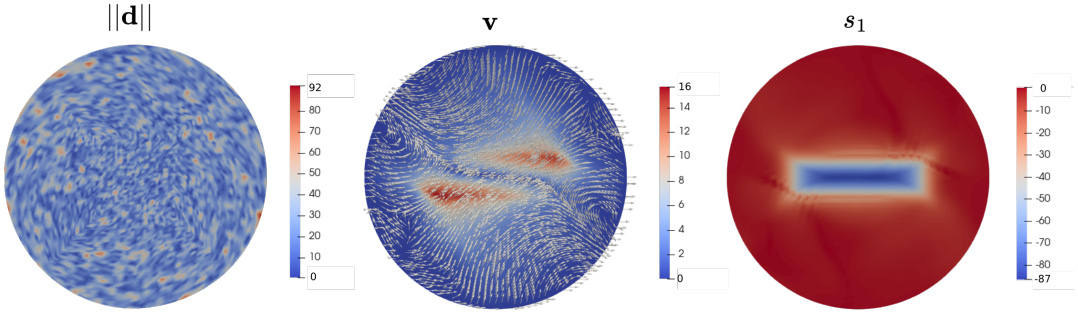

FIG. S8. Random disturbance rejected by the control action. Control settings are the same as in Fig. 2 in the main text.

- This m^*, and the induced s_1^*, guarantee that particles (or cells) will accumulate over short times to the short-time attractor as shown, e.g., in Fig. 1c and 2.
- If the disturbance forces $\mathbf{d}$ and boundary conditions do not change over time, then m^* will be the same over time. Otherwise, m^* must be recalculated accounting for the new $\mathbf{d}$ and boundary conditions to ensure the desired short-time attractor over the subsequent short-time interval.

We now illustrate our approach on an example of avian morphogenesis (as in Fig. 1), whose biological and physical details are available in [8, 9]. During gastrulation, the chick embryo is a confluent two-dimensional circular epithelium surrounded by co-planar extra-embryonic cells (Fig. S9a). Given the high viscosity of the tissue, inertia forces are negligible, and the viscous forces are balanced by active ones generated by actomyosin cables that contract with intensity m along ϕ (Eq. 1). Extra-embryonic cells migrate outward on a substrate, generating an outward velocity of the extra-embryonic tissue [10, 11]. This traction force is an imposed force from extraembryonic edge cells that the embryo cannot control [12], which, in our framework (Eqs. 2-3), we called $\mathbf{d}$. Because short-time attractors are defined from the instantaneous s_1 field at each t, and viscosity-dominated active nematics (Eq. 1) do not have an acceleration term (inertia is negligible), at each t the OCP generates an optimal distribution of m given $\mathbf{d}$ and boundary conditions. Therefore, as in all viscosity-dominated active nematic flows associated with morphogenesis, time is effectively a parameter in the force balance equation, and at each t, the tissue-scale $\mathbf{v}$ results from the balance between vis-

cous and current active and disturbance forces. We now ask how the embryo would modulate $m(\mathbf{x})$ to achieve a desired short-time attractor configuration $z(\mathbf{x})$, subject to the imposed $\mathbf{d}(\mathbf{x})$ at a given time.

We seek the optimal distribution of m for the embryo to generate a ring-shaped short-time attractor (z in Fig. S9c inset) close to the embryonic boundary subject to the imposed $\mathbf{d}$. The choice of z is motivated by recent experiments displaying that chick embryos can be molecularly perturbed to display a circular attractor (Fig 4F of [8]) instead of the linear one called Primitive Streak (see Fig. 1) observed in the wild-type embryos. In these experiments, we observed that the actomyosin cables are approximately tangential (Fig 4 of [9]), thus we set ϕ tangentially, as in Fig. S3 right. As in [8], because $\mathbf{d}$ acts on the thin outer edge of extraembryonic cells, causing them to move outward with a constant velocity, we model this effect by changing the boundary condition of the control problem (Eqs. 2-3) to a nonzero value and set $\mathbf{v_b} = v_b\mathbf{n}$, $v_b = 0.2$, where $\mathbf{n}$ is the normal direction to the boundary and the value of v_b (in nondimensional units) is consistent with experiments [8]. To reflect the purely contractile activity of actomyosin cables in chick morphogenesis, we modify the OCP enforcing $m \geq 0$.

Solving our modified OCP (Eqs. 2-3), we obtain the optimal m^* (Fig. S9b) and the corresponding optimal s_1^* (c), displaying the desired circular short-time attractor. Remarkably, this optimal solution is consistent with the myosin distribution and attractor configuration achieved in experiments. Specifically, by adding FGF2 (fibroblast growth factor 2) to chick embryos, we were able to generate a circular ring of active myosin m (Fig. S9d) as explained in detail in [9]. This control is indirect in that adding FGF2 induces a ring of mesoderm cells, which in turn generate active myosin. This ring distribution of m (d), resembling the optimal one from our model (b), strikingly generates a circular short-time attractor in the chick embryo. To see this, we image the velocity field of perturbed chick embryo in (d) and compute the s_1 field shown in (e), which is consistent with (c). For comparison, the uncontrolled (wild-type) chick embryo develops a straight short-time attractor shown in Fig. 1. These results show promising evidences that it is possible to control short-time attractors in-vivo in chick embryos. While controlling m in living embryos has limitations, a highly active field of research is developing mechanochemical and genetic manipulation techniques toward this goal [13–16]. Therefore, we expect our work to guide and benefit these experimental advances even more in the near future, progressing our understanding of morphogenesis mechanisms in living systems, and engineering synthetic ones.

* mserra@ucsd.edu.

[1] S. Salsa, *Partial differential equations in action: from modelling to theory*, Vol. 99 (Springer, 2016).

[2] R. A. Horn and C. R. Johnson, *Matrix analysis* (Cambridge university press, 2012).

[3] D. Arndt, W. Bangerth, B. Blais, M. Fehling, R. Gassmöller, T. Heister, L. Heltai, U. Köcher, M. Kronbichler, M. Maier, P. Munch, J.-P. Pelteret, S. Proell, K. Simon, B. Turcksin, D. Wells, and J. Zhang, The `deal.II` library, version 9.3, Journal of Numerical Mathematics **29**, 171 (2021).

[4] S. G. Johnson, *The NLopt nonlinear-optimization package* (2011).

[5] M. Gurtin, *An introduction to continuum mechanics*, Vol. 158 (Academic press, 1982).

[6] M. Serra and G. Haller, Objective eulerian coherent structures, Chaos: An Interdisciplinary Journal of Nonlinear Science **26**, 053110 (2016).

[7] B. Chachuat, *Nonlinear and dynamic optimization: From theory to practice*, Tech. Rep. (2007).

[8] M. Serra, G. Serrano Nájera, M. Chuai, A. M. Plum, S. Santhosh, V. Spandan, C. J. Weijer, and L. Mahadevan, A mechanochemical model recapitulates distinct vertebrate gastrulation modes, Science Advances **9**, eadh8152 (2023).

[9] M. Chuai, G. Serrano Nájera, M. Serra, L. Mahadevan, and C. J. Weijer, Reconstruction of distinct vertebrate gastrulation modes via modulation of key cell behaviors in the chick embryo, Science Advances **9**, eabn5429 (2023).

[10] D. New, The adhesive properties and expansion of the chick blastoderm, Development **7**, 146 (1959).

[11] H. C. Lee, Y. Fadaili, and C. D. Stern, Molecular characteristics of the edge cells responsible for expansion of the chick embryo on the vitelline membrane, Open Biology **12**, 220147 (2022).

[12] J. Downie, The mechanism of chick blastoderm expansion, Development **35**, 559 (1976).

[13] G. Guglielmi, J. D. Barry, W. Huber, and S. De Renzis, An optogenetic method to modulate cell contractility during tissue morphogenesis, Developmental cell **35**, 646 (2015).

[14] E. Izquierdo, T. Quinkler, and S. De Renzis, Guided morphogenesis through optogenetic activation of rho signalling during early drosophila embryogenesis, Nature communications **9**, 2366 (2018).

[15] H. J. Gustafson, N. Claussen, S. De Renzis, and S. J. Streichan, Patterned mechanical feedback establishes a global myosin gradient, Nature Communications **13**, 7050 (2022).

[16] H. Guo, M. Swan, and B. He, Optogenetic inhibition of actomyosin reveals mechanical bistability of the mesoderm epithelium during drosophila mesoderm invagination, ELife **11**, e69082 (2022).

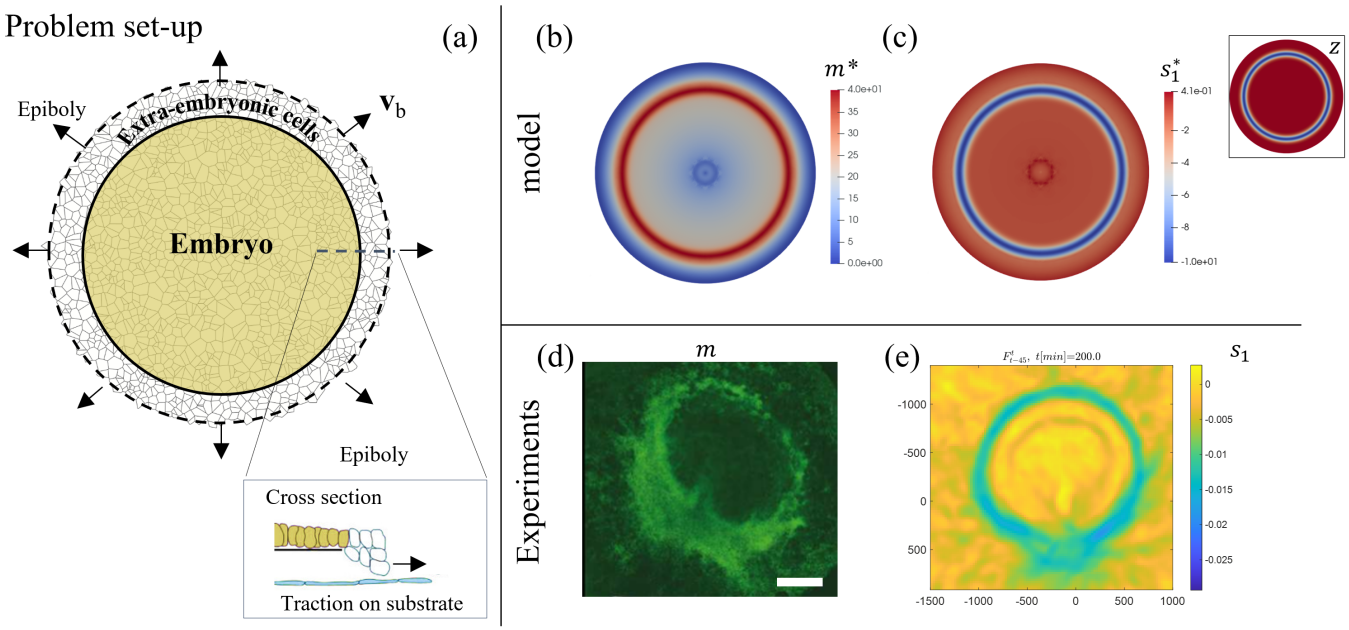

FIG. S9. Application to avian morphogenesis. (a) Sketch of the chick embryo during gastrulation, as described in Fig. 1. The embryo is a confluent disk-shaped epithelium where viscous forces balance active forces generated by actomyosin cables (Eq. 1). Extraembryonic cells are coplanar to the embryo and the outermost edge cells migrate outwards exerting traction forces on the substrate, generating a constant-velocity outward motion called epiboly. These traction forces are imposed on and cannot be controlled by the embryo. We ask what the optimal m^* distribution, controlled by embryonic cells, would be to generate a circular short-time attractor subject to the epiboly forces. (b) Optimal m^* solution of the OCP (Eqs. 2-3) with parameters $p_0 = 6$, $p_1 = 0.15$, control weight $\beta = 10^{-6}$, and boundary condition $\mathbf{v_b} = v_b\mathbf{n}$, $v_b = 0.2$, where $\mathbf{n}$ is the normal direction to the boundary. (c) Optimal s_1^* solution of the OCP, marking a short-time circular attractor. The inset shows the target s_1 distribution z using the same colorbar of s_1 (in nondimensional units). (d) Experimental distribution or mesendoderm cells, i.e., cells that generate more active myosin in a chemically perturbed (controlled) chick embryo ([9] for details). The scale bar is $500\mu m$, and brighter colors indicate more active myosin. (e) Experimental s_1 field in a chick embryo subject to the same perturbation shown in d marks a circular short-time attractor. Axes are in μm, the colormap marks attraction rates $(1/min)$. For comparison, the wild-type (uncontrolled) chick embryo develops a linear short-time attractor (Fig. 1).